Journal of Zhejiang University-SCIENCE A (Applied Physics & Engineering) 2023 24(1):56-63
www.jzus.zju.edu.cn; www.springer.com/journal/11582
E-mail: jzus_a@zju.edu.cn

Correspondence
https://doi.org/10.1631/jzus.A2200203

Finite volume method-based numerical simulation method for hydraulic fracture initiation in rock around a perforation

Yu ZHANG[1✉], Shaohao HOU[1], Songhua MEI[2], Yanan ZHAO[2], Dayong LI[1]

[1]College of Pipeline and Civil Engineering, China University of Petroleum (East China), Qingdao 266580, China
[2]Hunan Provincial Key Laboratory of Key Technology on Hydropower Development, Zhongnan Engineering Corporation, Changsha 410014, China

1 Introduction

Hydraulic fracturing is a technique for increasing permeability in oil and gas resource development, grouting reinforcement in mine management, and geo-stress measurement. For the purpose of enhancing hydraulic fracturing in horizontal wells, oriented perforating methods have been developed (Kurdi, 2018; Michael and Gupta, 2020a; Yan et al., 2020). Fluid is injected into the rock through perforations, which increases fluid pressure within rock and decreases rock temperature. Then, the rock around the perforation is fractured. Therefore, fracture initiation pressure is intimately connected to the reservoir's physical and mechanical properties, geo-stress, and temperature (Morgan and Aral, 2015). Accurate prediction of fracture initiation pressure is crucial in the design and construction of hydraulic fracturing systems (Zeng et al., 2018; Michael and Gupta, 2020b). Understanding the properties of the reservoir and state of stress around the wellbore is an effective method to predict fracture initiation.

Kurashige (1989) proposed a thermo-poro-elastic model based on Biot's pore-elasticity model considering thermal effects. The Kurashige model was used to analyze the effect of stress distribution around the wellbore on fracture initiation. A thermo-poro-elastic model that accounts for the effect of convective heat transfer was developed by Farahani et al. (2006), in which transient coupled pore pressure and temperature equations for non-isothermal conditions were developed based on conservation laws. Furthermore, Wang and Dusseault (2003) used a thermo-poro-elastic model that accounted for the coupling of heat conduction and thermal convection to calculate the shear stresses on the surface of a linear elastic porous medium around a wellbore. However, although thermo-pore-elastic models have been applied to vertical or inclined wellbores (Nguyen et al., 2010), they have rarely been applied to perforations. Most models ignore the impact of convective heat transfer from fluid flow, assuming that only conduction causes heat transfer from the wellbore to the reservoirs.

Because the maximum principal stress is from the overlying rock pressure, perforations drilled in the direction of the maximum horizontal principal stress are more susceptible to fracture initiation (Zhou et al., 1996). Russell et al. (2006) investigated the Tullich oil field, where the maximum principal stress is the overlying rock pressure, and drew similar conclusions. Zhang et al. (2017) studied the effects of geostatic stress, fluid injection rate, and perforation parameters on the hydraulic fracturing process with a modified particle flow code (PFC) model. Morgan and Aral (2015) studied the propagation of fracturing fluids in impermeable media with a finite volume fracture network model and verified the model by comparison with the results of a hydraulic fracturing experiment. Wellbore diameter, azimuth, and inclination angle are significant controllable parameters in the study of fracture initiation in horizontal wells. These studies considered the effects of stress or stress-flow coupling on the perforation well, but rarely considered thermal effects.

✉ Yu ZHANG, zhangyu@upc.edu.cn
Yu ZHANG, https://orcid.org/0000-0002-0179-6771

Received Apr. 13, 2022; Revision accepted Oct. 24, 2022; Crosschecked Jan. 4, 2023

The mechanical properties of rocks at high temperatures are related to their deformation and strength characteristics. Mechanical parameters such as elasticity modulus and Poisson's ratio vary in relation to temperature. An experimental study was conducted on the thermoelastic deformation of rock around a wellbore under a triaxial stress state from 20 to 600 °C to study the variation of the elastic modulus and Poisson's ratio with temperature (Xi and Zhao, 2010). From room temperature to 200 °C, the elastic modulus decreased by an average of 0.036 GPa per 1 °C increase, and Poisson's ratio increased from 0.25 to 0.35. The effective stress is the overall effect of normal stress and pore pressure. Mathematical relationships between the effective stress and permeability were established by fitting experimental data with the effective stress as the variable and stress sensitivity models for the reservoir (Wu et al., 2019; Hu et al., 2020). However, few results have been applied to the study of hydraulic fracturing.

In this study, a thermo-poro-elastic model is applied to horizontal perforation with consideration of the interactions of fluid flow and heat transfer. A numerical method based on finite volume method (FVM) is proposed for simulating fracture initiation of the rock around a perforation considering the stress sensitivity. The simulation verifies the correctness of the method for two types of situations. To analyze fracture initiation of perforations more accurately, the variation of elastic modulus and Poisson's ratio with temperature is included.

2 Theoretical model

2.1 Thermo-poro-elastic model

Deep oil and gas reservoirs are found in high temperature, high pressure, and high geo-stress conditions. Therefore, a thermo-poro-elastic model was obtained by superposing in-situ mechanical, hydraulic, and thermal induced stress effects. The detailed process is described in Section S1 of electronic supplementary materials (ESM). The reservoir material was assumed in the model to be homogeneous and linearly elastic.

2.2 Governing equations of fluid flow and temperature

Temperature affects fluid flow with heat flux, which includes the rock heat transfer $-\lambda\nabla T$ and the heat flux by the fluid flow $C_\mathrm{w}\rho_\mathrm{w}vT$. The governing equation for the temperature field is obtained without the source term:

$$\lambda\nabla^2 T - C_\mathrm{w}\rho_\mathrm{w}\nabla T\nabla P = C\rho\frac{\partial T}{\partial t}, \tag{1}$$

where λ is the thermal conductivity, T is the temperature, P is the fluid pressure, t is the time, v is the flow rate, C_w and ρ_w are the specific heat capacity and density of water, and C and ρ are the specific heat capacity and density of the reservoir, respectively.

Based on the continuity equation of fluid flow and Darcy's law, the transient fluid flow equation is

$$\frac{K}{\mu}\nabla^2 P + D_\mathrm{T}\nabla^2 T = \left[\beta_0\phi + \alpha_0(1-\phi)\right]\frac{\partial P}{\partial t}, \tag{2}$$

where D_T is the average thermal diffusivity, α_0 is the compression coefficient of the porous medium, β_0 is the compression coefficient of the fluid, K is the permeability of reservoir, μ is Poisson's ratio, and ϕ is the effective porosity. The detailed process of calculation of the relevant parameters and their stress sensitivity analysis are described in Section S2 of ESM.

3 Numerical simulation method based on FVM

3.1 Numerical simulation simplification

The interactions of fluid flow and heat transfer must be considered in a thermo-poro-elastic model. For a cylindrical coordinate system, if the interaction and polar angle are not related, decoupling the interaction of fluid flow and heat transfer can be carried out in 2D by applying an axisymmetric method. Thermally induced stress and hydraulic induced stress are not affected by the polar angle. Furthermore, the effect of stress on fluid flow is also independent of the polar angle because the stress uses the average stress. The effect of stress on heat transfer is not considered. Therefore, decoupling the interaction of fluid flow and heat transfer is simplified to a 2D question.

3.2 Spatial and time discretization

The wellbore is arranged vertically while intersecting the perforation, and the perforation are horizontal well. A quarter of the rock around the wellbore and perforation is selected for numerical simulation validation. The wellbore diameter is 5 mm, the perforation diameter 1 mm, and the length 4 mm. The model size is 50 mm×50 mm, which is divided into 100×100 meshes (Fig. S3). The injection fluid is water and the flow rate is 25 mL/min. The time increment is 0.001 s. The simulation parameters are detailed in Table S1.

The discrete equation of fluid flow is obtained by integrating the partial differential equation:

$$\begin{aligned}&\iiint [\beta_0\phi+\alpha_0(1-\phi)]\frac{\partial P}{\partial t}\mathrm{d}x\mathrm{d}y\mathrm{d}t=\\&\quad[\beta_0\phi^t+\alpha_0(1-\phi)^t]_U(P_U^{t+\Delta t}-P_U^t)\Delta x\Delta y,\end{aligned}\tag{3}$$

$$\begin{aligned}&\iiint \frac{K}{\mu}\nabla^2P+D_{\mathrm{T}}\nabla^2T\mathrm{d}x\mathrm{d}y\mathrm{d}t=\\&\quad\sum\frac{K}{\mu}\nabla P|S|+\sum D_{\mathrm{T}}\nabla T|S|,\end{aligned}\tag{4}$$

where $\frac{K}{\mu}\nabla P=\frac{K}{\mu}\frac{P_A-P_U}{|d|}$, $D_{\mathrm{T}}\nabla T=D_{\mathrm{T}}\frac{T_A-T_U}{|d|}$, and the subscript U is the center of the calculation, A is the nearest point to the center, including the four directions, N, S, W, and E (Fig. S4), Δx and Δy represent the time increments, $|d|$ is the distance from point A to U, and $|S|$ is the area of the calculation. Therefore,

$$\begin{aligned}&[\beta_0\phi^t+\alpha_0(1-\phi)^t]_U(P_U^{t+\Delta t}-P_U^t)\Delta x\Delta y=\\&\quad|S|\Big(a_UP_U+\sum a_AP_A+b_UT_U+\sum b_AT_A\Big),\end{aligned}\tag{5}$$

where a and b are coefficients, $a_A=\frac{K}{\mu}\frac{1}{|d|}$, $a_U=\sum(-a_A)$, $b_A=D_{\mathrm{T}}\frac{1}{|d|}$, $b_U=\sum(-b_A)$, and $a_U^t=[\beta_0\phi^t+\alpha_0(1-\phi)^t]_U\frac{\Delta x\Delta y}{|S|}$.

The discrete equation of temperature is

$$\iiint C\rho\frac{\partial T}{\partial t}\mathrm{d}t\mathrm{d}y\mathrm{d}x=(C\rho)_U(T_U^{t+\Delta t}-T_U^t)\Delta x\Delta y,\tag{6}$$

$$\begin{aligned}&\iiint \lambda\nabla^2T-C_{\mathrm{w}}\rho_{\mathrm{w}}\nabla T\nabla P\mathrm{d}x\mathrm{d}y\mathrm{d}t=\\&\quad\sum\lambda(\nabla T)|S|+\sum C_{\mathrm{w}}\rho_{\mathrm{w}}T(\nabla P)|S|,\end{aligned}\tag{7}$$

where $\lambda\nabla T=\lambda\frac{T_A-T_U}{|d|}$, and $C_{\mathrm{w}}\rho_{\mathrm{w}}T\nabla P=C_{\mathrm{w}}\rho_{\mathrm{w}}T\frac{P_A-P_U}{|d|}$.

Therefore,

$$\begin{aligned}&(C\rho)_U(T_U^{t+\Delta t}-T_U^t)\Delta x\Delta y=\\&\quad|S|\Big(c_UT_U+\sum c_AT_A+d_UP_U+\sum d_AP_A\Big),\end{aligned}\tag{8}$$

where c and d are coefficients, $c_A=\lambda\frac{1}{|d|}$, $c_U=\sum(-c_A)$, $d_A=C_{\mathrm{w}}\rho_{\mathrm{w}}T_A\frac{1}{|d|}$, $d_U=\sum(-d_A)$, and $c_U^t=(C\rho)_U\frac{\Delta x\Delta y}{|S|}$.

3.3 Iterative algorithm

The stress $\sigma^{t+\Delta t}$ is a function of fluid pressure in the wellbore $P_{\mathrm{w}}(t)$, with porosity ϕ^t, fluid pressure P^t, and temperature T^t in the reservoir. The iterative formula is as follows:

$$\sigma^{t+\Delta t}=f(P_{\mathrm{w}}(t),\phi^t,P^t,T^t),\tag{9}$$

and the corresponding parameters also need to be iterated:

$$K^{t+\Delta t}=K_0\mathrm{e}^{-M(\sigma^t-\alpha^tP^t)},\tag{10}$$

$$\phi^{t+\Delta t}=\phi_0\mathrm{e}^{-\frac{M(\sigma^t-\alpha^tP^t)}{3}},\tag{11}$$

where K_0 is the initial permeability, M is the stress sensitivity factor of permeability, ϕ_0 is the initial porosity, and σ is the average stress.

For non-Darcy flow, the permeability should be corrected for:

$$K_{\mathrm{N}}^{t+\Delta t}=\frac{K^t}{1+\frac{\beta^{t+\Delta t}\rho_{\mathrm{w}}K^tv^{t+\Delta t}}{\mu}}.\tag{12}$$

Therefore, a numerical simulation method based on FVM for hydraulic fracturing is proposed (Fig. S5), which includes the fluid pressure, fracture initiation pressure, fracture initiation location, and fracture initiation time.

3.4 Simulation setup and boundary conditions

There are three boundary conditions to be resolved in this model: a symmetric boundary, inner boundary, and outer boundary (Fig. S6).

No fluid crosses the symmetrical boundary ($a_{\mathrm{sym}}=0$). The nodes $(\delta x)_W$ and $(\delta y)_S$, next to the inner boundary are half of the original (Fig. S7): $a_{\mathrm{in}}=\frac{1}{2}a$, $b_{\mathrm{in}}=\frac{1}{2}b$,

$c_{\text{in}} = \frac{1}{2}c$, and $d_{\text{in}} = \frac{1}{2}d$, and the subscript "in" means the inner boundary.

The outer boundary nodes of the model are macroscopic internal nodes for the reservoir. Therefore, a nodal algebraic equation is added outside the boundary to modify the nodal coefficients of the outer boundary.

$$\begin{cases} P_M = \dfrac{P_{M+1} + P_{M-1}}{2}, \quad a_{M+1} = a_M, \\ T_M = \dfrac{T_{M+1} + T_{M-1}}{2}, \quad c_{M+1} = c_M, \end{cases} \tag{13}$$

where the subscript M is the point of outer boundary, M+1 and $M-1$ represent the internal and external points next to the node M, respectively.

The fluid pressure and temperature in the wellbore and perforation are always $P_{\text{in}}(t)=P_{\text{w}}(t)$ and $T_{\text{in}}(t)=T_{\text{w}}(t)$, respectively. The reservoir temperature gradient is 3.6 °C/100 m. At the start of fluid flow (t=0), the fluid pressure at any location within the reservoir is considered to be the initial pore pressure (i.e., $P(r, 0)=P_0$). The temperature at the horizontal height of the perforation is 135 °C.

4 Results and discussion

4.1 Model validation

To verify the accuracy of the constructed model, the Hubbert–Willi (H-W) and Haimson–Fairhurst (H-F) models were introduced. The H-W model gives an upper limit value of the fracture initiation pressure without considering the permeability of rock around the perforation, while the H-F model gives a lower limit value with high permeability. The H-W model is given by

$$P_{\text{b}} = 3\sigma_{\text{h}} - \sigma_{\text{H}} + \sigma_{\text{t}} + P_0, \tag{14}$$

where σ_{H} and σ_{h} are the horizontal maximum and minimum principal stresses, respectively, σ_{t} is the tensile strength, P_0 is the initial pressure, and P_{b} is the fracture initiation pressure.

The H-F model is given by

$$P_{\text{b}} = \frac{3\sigma_{\text{h}} - \sigma_{\text{H}} + \sigma_{\text{t}} - 2\eta P_0}{2(1-\eta)}, \tag{15}$$

where $\eta = \dfrac{\phi(1-2\mu)}{2(1-\mu)}$.

The fracture initiation pressure is 75.67 MPa in the H-W model and 40.18 MPa in the H-F model. In this study, the minimum fracture initiation pressure is 40.95 MPa when the wellbore wall is permeable and the maximum is 58.22 MPa when the wellbore wall is impermeable. All fracture initiation pressure results are intermediate in relation to the H-W and H-F models, which indicates that the model is correct.

4.2 Results analysis

4.2.1 Effects of the perforation azimuth

Fig. 1a shows that the fracture initiation pressure is higher when the wellbore wall is impermeable than when it is permeable, and the pressure increases with the rise of the perforation azimuth. The minimum fracture initiation pressure is 41.58 MPa when θ=0° and the wellbore is impermeable. The fracture initiation pressure increases rapidly between 0° and 60°. Beyond

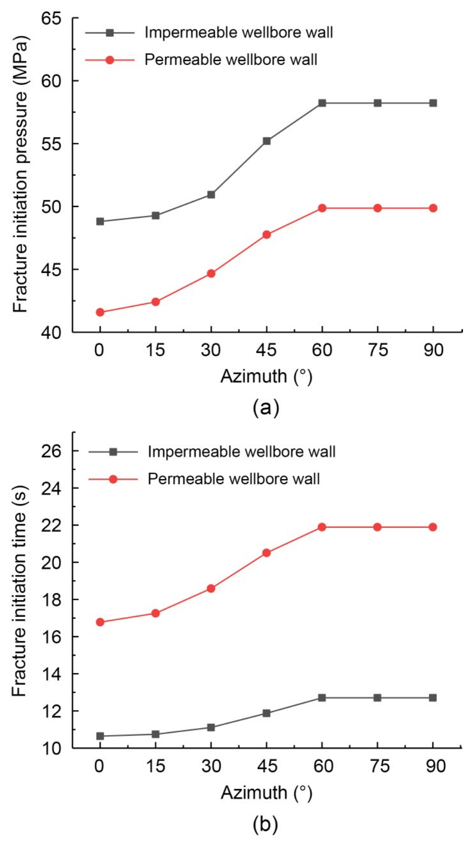

Fig. 1 Fracture initiation of rock around a perforation under different perforation azimuths: (a) fracture initiation pressure; (b) fracture initiation time

60°, the pressure remains almost constant and maintains a weak relationship with the perforation azimuth.

The patterns of crack initiation time and crack initiation pressure are similar (Fig. 1b). As the perforation azimuth rises, more injection time is required to reach fracture initiation at azimuth angles of less than 60°. Beyond 60°, the time remains a constant. Compared to when the wellbore wall is permeable, the fracture initiation time curve is flatter when the wellbore wall is impermeable, which indicates a more rapid pressure increase.

4.2.2 Effect of the stress sensitivity of permeability and porosity

When stress sensitivity is present, both fracture initiation pressure and time are reduced (Fig. 2). The greater the perforation azimuth, the more noticeable the reduction in fracture initiation time. The fracture initiation pressure reduction is not significant.

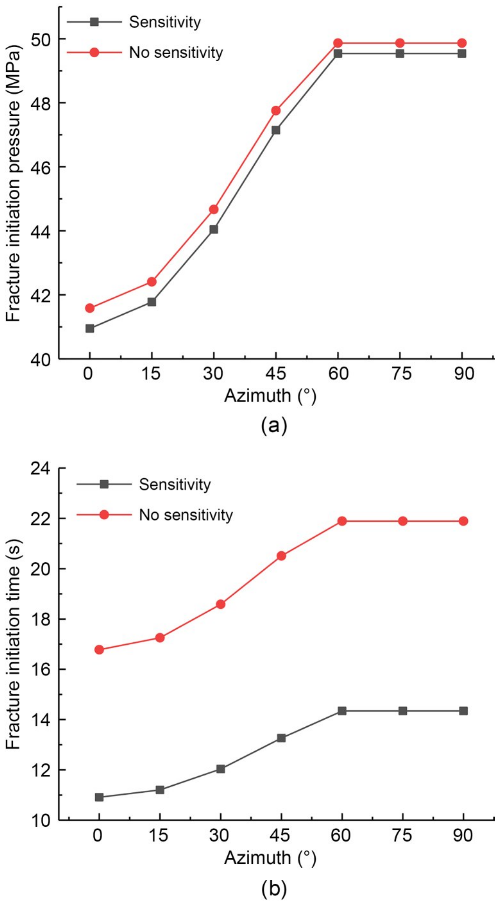

Fig. 2 Fracture initiation of rock around perforation when the wellbore wall is permeable: (a) fracture initiation pressure; (b) fracture initiation time

4.2.3 Distributions of fluid pressure and temperature

Figs. 3 and 4 show the distributions of fluid pressure and temperature when θ=0°. Fluid pressure is distributed in an ellipse next to the perforation and reduces gradually from the perforation to the far field when the wellbore wall is impermeable. When the wellbore wall is permeable, the fluid pressure distribution is spread outwards along the wellbore because fluid flows into the reservoir from the wellbore. The temperature distribution around the wellbore and perforation is similar to the fluid pressure. However, the reservoir temperature increases gradually from the perforation to the far field.

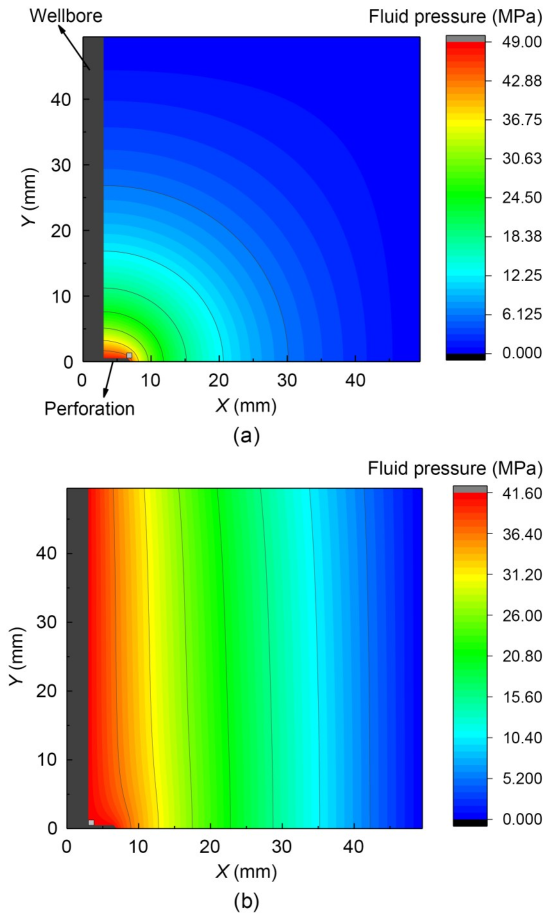

Fig. 3 Fluid pressure distribution when fracture initiates (θ=0°): (a) impermeable wellbore wall; (b) permeable wellbore wall. The grey point represents the fracture initiation location. References to color refer to the online version of this figure

For θ=0°, the fracture initiation location is at the top of the perforation when the boundary is impermeable, and at the end of the perforation when it is

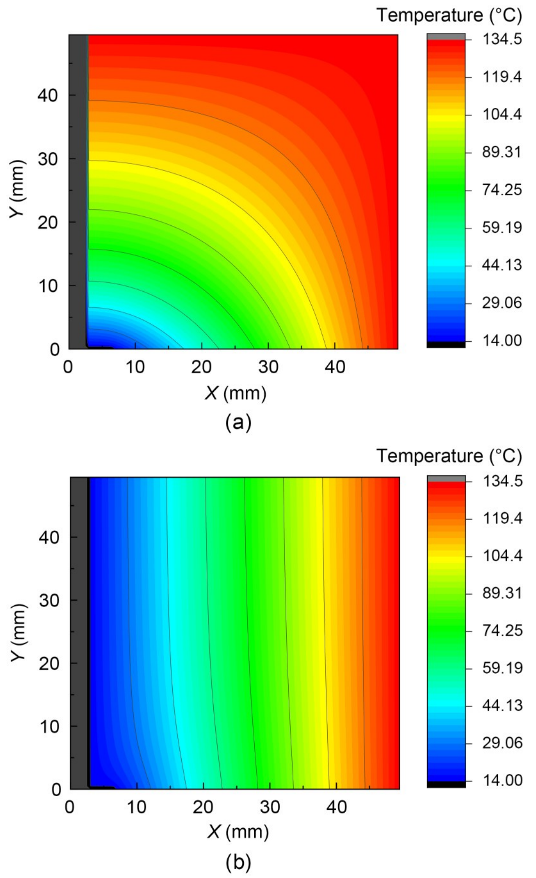

Fig. 4 Temperature distribution when fracture initiates (θ=0°): (a) impermeable wellbore wall; (b) permeable wellbore wall

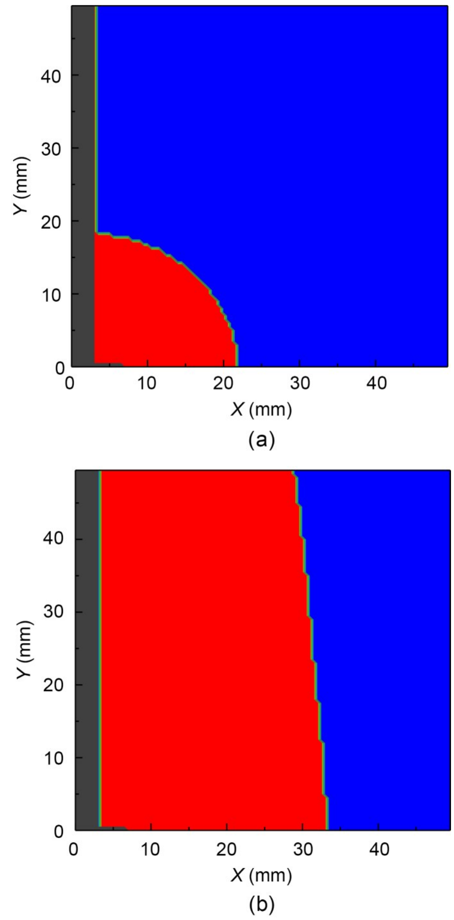

Fig. 5 Darcy and non-Darcy areas when fracture initiates (θ=0°): (a) impermeable wellbore wall; (b) permeable wellbore wall. The red represents non-Darcy area; the blue represents the Darcy area. References to color refer to the online version of this figure

permeable. The compressive stress of the reservoir around the top of perforation is induced, which reduces the fracture initiation pressure, and the location of the fracture initiation is at the top of the perforation. However, when $\theta \geqslant 60°$ the fracture initiation location shifts to the perforation wall of the maximum horizontal stress direction, with either an impermeable or permeable boundary.

The Darcy area is distributed in an ellipse next to the perforation when the wellbore wall is impermeable (Fig. 5). When the wellbore wall is permeable, the Darcy area is like a right-angle trapezoid shape because the perforation channel enhances the flow distance.

4.2.4 Distribution of permeability

Fig. 6 shows the distribution of permeability when θ=0°. The permeability above the perforation is higher than at the same horizontal height when the wellbore wall is impermeable, because the fluid pressure in the perforation is higher than others at the same height. The permeability distribution is spread outwards along the wellbore similar to the temperature distribution when the wellbore is permeable. The increasing permeability in the near-well area causes an increase in flow rate and a wider range of fluid flow.

5 Conclusions

1. As the perforation azimuth rises, a longer injection time and higher fluid pressure are required to reach fracture initiation. The fracture initiation pressure is higher when the wellbore wall is impermeable than when it is permeable.

2. Fluid pressure is distributed in an ellipse next to the perforation and reduces gradually from the perforation to the far field when the wellbore wall is

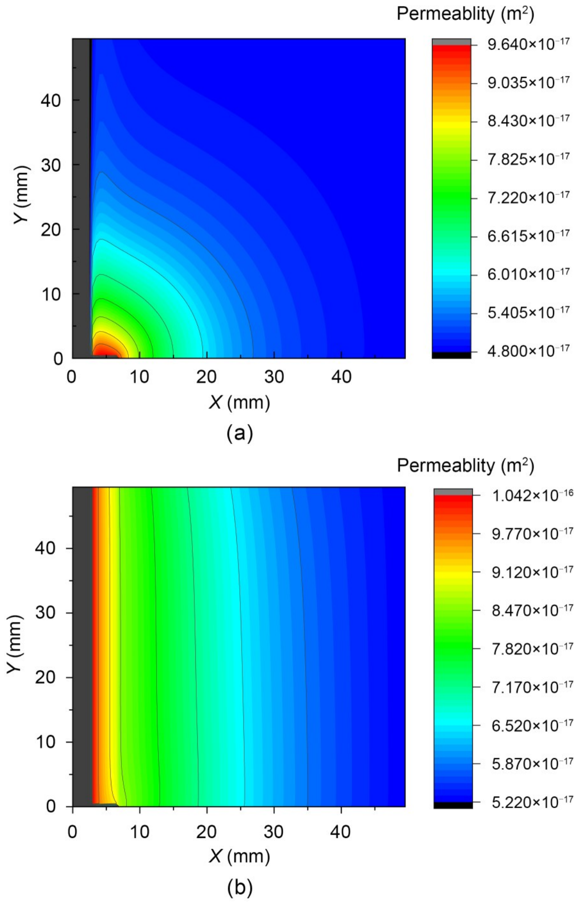

Fig. 6 Distribution of permeability when fracture initiates (θ=0°): (a) impermeable wellbore wall; (b) permeable wellbore wall

impermeable. When the wellbore wall is permeable, the fluid pressure distribution is spread outwards along the wellbore because fluid flows into the reservoir from the wellbore.

3. The stress sensitivity of permeability and porosity increases fluid pressure and permeability in the area around the well, which causes a wider range of fluid flow and a reduction in both fracture initiation pressure and time.

Acknowledgments

This work is supported by the National Natural Science Foundation of China (Nos. 51890914 and 52179119), the Natural Science Foundation of Shandong Province (No. ZR2019MEE001), and the Open Research Fund of Hunan Provincial Key Laboratory of Hydropower Development Key Technology (No. PKLHD202001), China.

Author contributions

Yu ZHANG designed the research. Shaohao HOU and Songhua MEI processed the corresponding data. Yu ZHANG wrote the first draft of the manuscript. Yanan ZHAO helped to organize the manuscript. Shaohao HOU and Dayong LI revised and edited the final version.

Conflict of interest

Yu ZHANG, Shaohao HOU, Songhua MEI, Yanan ZHAO, and Dayong LI declare that they have no conflict of interest.

References

Farahani H, Yu M, Miska S, et al., 2006. Modeling transient thermo-poroelastic effects on 3D wellbore stability. SPE Annual Technical Conference and Exhibition. https://doi.org/10.2118/103159-MS

Hu Z, Klaver J, Schmatz J, et al., 2020. Stress sensitivity of porosity and permeability of Cobourg limestone. *Engineering Geology*, 273:105632. https://doi.org/10.1016/j.enggeo.2020.105632

Kurashige M, 1989. A thermoelastic theory of fluid-filled porous materials. *International Journal of Solids and Structures*, 25(9):1039-1052. https://doi.org/10.1016/0020-7683(89)90020-6

Kurdi M, 2018. A new computational model to predict breakdown pressures in cased and perforated wells in unconventional reservoirs. SPE Annual Technical Conference and Exhibition. https://doi.org/10.2118/194038-STU

Michael A, Gupta I, 2020a. Analytical orientation criteria for drilling and completion-induced fracture initiation considering fluid infiltration from the wellbore. *Journal of Petroleum Science and Engineering*, 190:107033. https://doi.org/10.1016/j.petrol.2020.107033

Michael A, Gupta I, 2020b. A semi-analytical modeling approach for hydraulic fracture initiation and orientation in shale reservoirs. Proceedings of the 8th Unconventional Resources Technology Conference. https://doi.org/10.15530/urtec-2020-3137

Morgan WE, Aral MM, 2015. An implicitly coupled hydrogeomechanical model for hydraulic fracture simulation with the discontinuous deformation analysis. *International Journal of Rock Mechanics and Mining Sciences*, 73:82-94. https://doi.org/10.1016/j.ijrmms.2014.09.021

Nguyen D, Miska S, Yu MJ, et al., 2010. Modeling thermal effects on wellbore stability. Trinidad and Tobago Energy Resources Conference. https://doi.org/10.2118/133428-MS

Russell KA, Ayan C, Hart NJ, et al., 2006. Predicting and preventing wellbore instability: Tullich field development, North Sea. *SPE Drilling & Completion*, 21(1):12-22. https://doi.org/10.2118/84269-PA

Wang Y, Dusseault MB, 2003. A coupled conductive–convective thermo-poroelastic solution and implications for wellbore stability. *Journal of Petroleum Science and Engineering*, 38(3-4):187-198. https://doi.org/10.1016/S0920-4105(03)00032-9

Wu Z, Cui C, Trivedi J, et al., 2019. Pressure analysis for volume fracturing vertical well considering low-velocity

non-Darcy flow and stress sensitivity. *Geofluids*, Article ID 2046061.
https://doi.org/10.1155/2019/2046061

Xi BP, Zhao YS, 2010. Experimental study of thermophysico-mechanical property of drilling surrounding rock in granite under high temperature and high pressure. *Chinese Journal of Rock Mechanics and Engineering*, 29(6):1245-1252 (in Chinese).

Yan X, Huang ZQ, Zhang Q, et al., 2020. Numerical investigation of the effect of partially propped fracture closure on gas production in fractured shale reservoirs. *Energies*, 13(20):5339.
https://doi.org/10.3390/en13205339

Zeng QD, Liu WZ, Yao J, 2018. Hydro-mechanical modeling of hydraulic fracture propagation based on embedded discrete fracture model and extended finite element method. *Journal of Petroleum Science and Engineering*, 167:64-77.
https://doi.org/10.1016/j.petrol.2018.03.086

Zhang LQ, Zhou J, Han ZH, 2017. Hydraulic fracturing process by using a modified two-dimensional particle flow code-case study. *Progress in Computational Fluid Dynamics, An International Journal*, 17(1):13.
https://doi.org/10.1504/PCFD.2017.081715

Zhou SH, Hillis RR, Sandiford M, 1996. On the mechanical stability of inclined wellbores. *SPE Drilling & Completion*, 11(2):67-73.
https://doi.org/10.2118/28176-PA

Electronic supplementary materials

Sections S1–S3